



Quantifying Brain [^{18}F]FDG Uptake Noninvasively by Combining Medical Health Records and Dynamic PET Imaging Data

Elisa Roccia , Arthur Mikhno , R. Todd Ogden, J. John Mann, Andrew F. Laine, Elsa D. Angelini, and Francesca Zanderigo

Abstract—Full quantification of regional cerebral metabolic rate of glucose (rCMRglu) with [^{18}F]fluorodeoxyglucose ([^{18}F]FDG) positron emission tomography (PET) imaging requires measurement of an arterial input function (AIF) curve, which is obtained with an invasive arterial blood sampling procedure during the scan. We previously proposed a non-invasive simultaneous estimation (nSIME) method that quantifies binding of a PET radioligand by combining individual electronic health records information and a pharmacokinetic AIF (PK-AIF) model. Initially applied only to [^{11}C]DASB data, in this study we validate nSIME for a different radioligand, [^{18}F]FDG, adapting the algorithm to the specific distribution and metabolism of this radioligand. We evaluate the impact of the PK-AIF model, the number of [^{18}F]FDG-specific soft constraints, and the type of predictive strategy. The accuracy of nSIME is then compared to a population-based approach. All analyses are conducted on 67 [^{18}F]FDG PET scans with arterial blood data available for comparison. nSIME performance is optimal for [^{18}F]FDG when using the PK-AIF model, two soft constraints, and an aggregate model to predict the soft constraint values. Higher correlation and lower Bland–Altman spread against

gold standard rCMRglu values based on arterial blood measurements are observed for nSIME ($r = 0.83$, spread = 1.55) compared to the population-based approach ($r = 0.77$, spread = 2.12). nSIME provides a data-driven estimation of both amplitude and shape of the AIF curve at the individual level and potentially enables non-invasive quantification of PET data across radioligands, avoiding the need for arterial blood sampling.

Index Terms—Arterial input function (AIF), electronic health record (EHR), positron emission tomography (PET).

I. INTRODUCTION

POSITRON emission tomography (PET) allows for *in vivo* measurement of tissue metabolism and neurochemistry [1], [2]. [^{18}F]fluorodeoxyglucose ([^{18}F]FDG) is a PET radioligand widely used to quantify glucose metabolism for the investigation, for example, of tumors and neurological disorders such as Alzheimer's disease [3]–[6].

Current gold standard full quantification of regional cerebral metabolic rate of glucose (rCMRglu) from [^{18}F]FDG PET data requires measuring an arterial input function (AIF), which is the radioligand concentration level in plasma over the duration of the scan, by assaying blood samples acquired from an arterial line during scanning. Insertion of an arterial line is a relatively invasive procedure with potential complications, and the subsequent blood assays are not always reliable, adding measurement errors. The procedure is costly, discomforting for the patient and exposes clinical staff to additional radiation. Consequently, approaches alternative to arterial blood sampling have been proposed [7]–[12].

Image-derived input function (IDIF) approaches have been proposed for [^{18}F]FDG [7], which recover the AIF directly from the PET images by identifying cranial blood pools in the field of view. These structures are limited in size, and their signal is sensitive to motion artifacts and partial volume effect. IDIF also requires a fast acquisition protocol of the PET images, to accurately recover the initial part of the AIF curve, and a few blood samples for calibration of the recovered IDIF. Alternatively, population-based input function (PBIF) approaches have been validated for [^{18}F]FDG [9]–[12], which derive a template AIF curve by normalizing individual AIF (obtained via arterial blood sampling) from a large population of subjects scanned with the same radioligand. The template is then individually calibrated to the subject using a scaling factor. PBIF methods rely on the assumption that the AIF has a constant shape across

Manuscript received May 22, 2018; revised October 18, 2018 and December 17, 2018; accepted December 21, 2018. Date of publication January 1, 2019; date of current version November 6, 2019. This work was supported in part by the National Institute of Mental Health F31 Pre-doctoral Fellowship (1F31MH095338) and in part by the National Center for Advancing Translational Sciences, National Institutes of Health, under Grant TL1 TR000082. (Elisa Roccia and Arthur Mikhno contributed equally to this work.) (Corresponding author: Arthur Mikhno.)

E. Roccia is with the School of Biomedical Engineering & Imaging Sciences, King's College London, King's Health Partners, St Thomas' Hospital, London, SE1 7EH, United Kingdom (e-mail: elisa.rocchia@kcl.ac.uk).

A. Mikhno and A. F. Laine are with the Department of Biomedical Engineering, Columbia University, New York, NY 10027 USA (e-mail: am2679@columbia.edu; al418@columbia.edu).

R. T. Ogden is with the Departments of Psychiatry and Biostatistics, Columbia University, New York, NY 10032 USA (e-mail: to166@columbia.edu).

J. J. Mann is with the Departments of Psychiatry and Radiology, Columbia University, New York, NY 10032 USA (e-mail: jjm@columbia.edu).

E. D. Angelini is with the Department of Biomedical Engineering, Columbia University, New York, NY 10027 USA, and also with the NIHR Imperial Biomedical Research Centre, ITMAT Data Science Group, Imperial College London, London SW7 2AZ, U.K. (e-mail: e.angelini@imperial.ac.uk).

F. Zanderigo is with the Department of Psychiatry, Columbia University, and the Molecular Imaging and Neuropathology Division, New York Psychiatric Institute, New York, NY 10032 USA (e-mail: fz2173@cumc.columbia.edu).

Digital Object Identifier 10.1109/JBHI.2018.2890459

2168-2194 © 2019 IEEE. Personal use is permitted, but republication/redistribution requires IEEE permission.
See http://www.ieee.org/publications_standards/publications/rights/index.html for more information.

subjects, but in fact, kinetic and metabolic profiles can vary across individuals [13], [14].

Simultaneous estimation (SIME) is another promising approach that has been validated [15] as an alternative, less invasive method for recovering the AIF. SIME is based on a mathematical model for the AIF, and estimates the free parameters of such model together with the parameters of the model that describes the radioligand kinetics in the tissue, by simultaneously fitting multiple brain regions at once. However, SIME still requires at least one blood sample to be included as a constraint within the algorithm cost function to ensure AIF identifiability. Instead of obtaining this blood sample, we have shown previously that it may be possible to predict the constraint variable from non-invasive patient information [16]. More recently, a fully non-invasive SIME (nSIME) framework was introduced that combines electronic health records (EHR) with dynamic PET data to estimate the AIF for [^{11}C]DASB, a radioligand used to image the serotonin transporter [17]. Differently from the original SIME [15], nSIME adds multiple soft constraints within the algorithm cost function, and predicts such constraint variables from EHR and PET data using pre-trained models, instead of deriving them from the subject blood sample.

The key innovation of this work is the application of nSIME for use with [^{18}F]FDG by adapting, optimizing, and validating the algorithm for this radioligand. The utility of EHR-based predictions needs in fact to be assessed for each radioligand, as the EHR variables predictive of its pharmacokinetics and metabolism are not known a priori, and can vary across radioligands. Preliminary results of this application were published in [18], which is expanded upon here with several new technical contributions: 1) comparison of nSIME to gold standard quantification; 2) rigorous characterization of both SIME and nSIME with one and two constraints using a more advanced predictive algorithm; 3) comparison of the proposed pharmacokinetic AIF model to the previously used 3-decreasing exponential model; 4) addition of an AIF curve shape selection procedure; and 5) benchmarking of nSIME against a non-invasive population based approach.

II. MATERIALS AND METHODS

A. Subjects and Associated Data

PET, EHR, and magnetic resonance imaging (MRI) data were acquired as part of a study of patients with mild cognitive impairment (MCI), mild Alzheimer's disease (AD) and age-matched healthy controls. The study was approved by the Institute Review Board of the New York State Psychiatric Institute and Columbia University [19]. EHR were collected prior to the PET scan and included demographics, clinical details, clinical laboratory test results, urinalysis, and vital parameters. PET data included regional brain time activity curves (TACs), injected dose of [^{18}F]FDG (ID), injected mass of [^{18}F]FDG, and radioligand specific activity. The AIF was determined using full arterial blood sampling. Eighty-nine PET scans were previously acquired from 58 subjects. Only scans with a fully sampled AIF, TACs and EHR were included in the final dataset, which includes 67 PET scans from 49 subjects. The 67 scans include 46 baseline and 21 follow-up assessments at ~ 1.5 years (Table I).

B. PET-Related Data Acquisitions and Pre-Processing

For details of the acquisition protocols, we refer to [19]. Briefly, PET images were acquired on an ECAT EXACT HR+

TABLE I
DESCRIPTIVE STATISTICS OF THE STUDY POPULATION:
67 TOTAL PET SCANS FROM 49 SUBJECTS

Variable	Mean (std)	Min	Max
Age (years)	68.7 (8.3)	51	87
Sex (# of Male/Female)	28 / 39		
Weight (kg)	74.3 (13.4)	49.0	106.1
Height (m)	1.67 (0.11)	1.36	1.91
Injected dose (MBq)	178.4 (9.9)	114	185
Time EHR-PET (days)	19.46 (18.70)	0	96
Diagnosis (# subjects): CTR/MCI/AD	23 / 25 / 19		
Scan (#): baseline / follow up	46 / 21		
Baseline – follow up time gap (years)	1.51 (0.31)	1.01	2.15

EHR = electronic health records, CTR = healthy controls, MCI = mild cognitive impairment, AD = Alzheimer's disease.

scanner (Siemens/CTI, Knoxville, TN). After a 10-minute transmission scan, a bolus injection of [^{18}F]FDG ($178.4 \text{ MBq} \pm 9.9 \text{ MBq}$ across scans) was administered intravenously. Emission data were acquired in 3D mode for 60 minutes with 26 frames of increasing duration. Images were reconstructed on a 128×128 matrix (pixel size $2.5 \times 2.5 \text{ mm}^2$), after attenuation and scatter correction. Fourteen arterial blood samples were drawn during scan. Samples were centrifuged and plasma radioactivity measured using a well counter. Cold glucose concentration in blood was measured by a glucometer before and after the PET scan, and values averaged. The prefrontal cortex (PFC), cingulate (CIN), hippocampus (HIP), parahippocampal gyrus (PIP) and grey matter cerebellum (CER) were labeled on MRI scans by a trained technician [20], [21]. Regions of interest (ROI) masks were transferred to motion-corrected and MRI co-registered PET images, and TACs extracted as average activity in each ROI over time. The sum of mean activity in the whole brain from 2.5 to 10 minutes post-injection (TACsum) was also derived. A preliminary analysis found that TACsum in this time window is strongly correlated to [^{18}F]FDG plasma concentration.

C. EHR Data

EHR include laboratory data on individual subjects that are used to compose a list of 83 initial predictors (Table II). EHR measures include demographics, clinical information, clinical laboratory test results (chemistry and hematology), urinalysis and vitals (HR, BP) pre- and post-PET scan. Average of pre- and post-PET scan values were added for HR, and systolic and diastolic blood pressure. Secondary measures derived from sex, age, height, weight, and hematocrit include body mass index (BMI), body surface area (BSA), estimated total blood volume (eTBV), estimated total plasma volume (eTPV), estimated resting metabolic rate (eRMR), pulse pressure (PP), mean arterial pressure (MAP), and estimated cardiac output (eCO), which approximates the stroke volume (SV). Glomerular filtration rate (eGFR) was calculated using blood urea nitrogen (BUN) and albumin (Albumin), and adjusted for individual BSA [22]. Standard clinical formulae were used for the calculation of albumin-corrected calcium (rCalcium), blood viscosity, anion gap, BUN:Creatinine (BUN:Crt) ratio and plasma osmolarity [17].

For each scan, a PBIF was also derived from height and weight according to the approach proposed in [23], and the area under the curve of such PBIF included as an additional potential

TABLE II
EHR PATIENTS' DATA USED IN THE PREDICTION OF THE
CONSTRAINT VARIABLES

Initial predictors (N = 83)			
Chemistry (24)	Hematology (19)	Derived (24)	Vitals (9)
A/G Ratio	BasoAbsolute	AnionGap	Bpd Avg
Albumin	Baso%	eCO Avg	Bpd PostScan
AlkPhos	EosinAbsolute	MAP Avg	Bpd PreScan
ALT(SGPT)	Eosin%	PP Avg	BPs Avg
AST(SGOT)	Hematocrit	Blood viscosity	BPs PostScan
BUN	Hemoglobin	BMI	BPs PreScan
Calcium	LymphAbsolute	BSA	HR Avg
Chloride	Lymph%	BUN:Crt ratio	HR PostScan
Cholesterol	MCH	eCO PostScan	HR PreScan
CO2	MCHC	eCO PreScan	
ColdGlu1	MCV	eGFR	PET (3)
ColdGlu2	MonoAbsolute	eGFRBSA	AUCpopul
Creatinine	Mono%	eGFR5	Injected Dose
Globulin	NeutAbsolute	eGFR5BSA	TACsum
Glucose	Neut%	eRMR	
LDH	Platelets	eTBV	Demographics (4)
MeanGlu	RBC	eTPV	Age
Phosphorus	RDW	LBMI	Height
Potassium	WBC	MAP PostScan	Sex
Sodium		MAP PreScan	Weight
T. Bilirubin		Plasma osmolarity	
Total Protein		PP PostScan	
Triglyceride		PP PreScan	
UricAcid		rCalcium	

predictor variable (AUCpopul). Of specific interest was whether this variable would be selected in the final predictive algorithm as part of the general comparison of nSIME against the PBIF approach.

D. Gold Standard rCMRglu

A two-tissue irreversible compartmental model is fit to each ROI TAC separately, using the arterial-blood-based AIF [24]. Estimates of the model free parameters are obtained by minimizing the error between measured data and TAC fit using a non-linear least squares estimator. rCMRglu is then calculated as a function of the model parameters.

E. Pharmacokinetic AIF Model

nSIME uses a mathematical model to describe the AIF (C_p), which is common across all brain ROIs. The free parameters of the AIF model are estimated together with those describing the radioligand kinetics in tissue by fitting TACs from multiple ROIs simultaneously. The original implementation of SIME [15] used a 3-decreasing exponential (3E-AIF) model, which fits a straight line to the peak (infusion phase), followed by a combination of three-exponentials after the peak (elimination phase). For nSIME, we employ a pharmacokinetic (PK) model for the AIF, where infusion and elimination phases are both non-linear and share parameters, for a more physiologically accurate description of drug delivery [17]. Specifically, we used the three-compartment PK model reported in Equation (1), where $\theta^{PK} = [B_l, \lambda_l, t_d, T]$ denotes the vector of free parameters of the model, B_l is a scaling constant, λ_l is the rate constant of the l^{th} compartment, t_d is the radioligand infusion delay and T is the infusion duration.

$$C_p^{PK}(t|\theta^{PK}) = \begin{cases} \sum_{l=1}^3 B_l (e^{-\lambda_l(t-t_d)} - 1), & t < T \\ \sum_{l=1}^3 B_l (e^{-\lambda_l T} - 1) e^{-\lambda_l(t-t_d)}, & t \geq T \end{cases} \quad (1)$$

The PK-AIF model was fitted to the arterial blood-derived measurements for all scans, to derive physiological ranges for the parameters in θ^{PK} , which are used as parameter bounds

(minimum and maximum values) and as initial parameter estimates (mean physiological values) within the nSIME algorithm.

F. Non-Invasive Simultaneous Estimation (nSIME)

Differently from the gold standard approach, SIME fits multiple TACs at once and requires only one blood sample acquired at some time point post-injection. The optimal sampling time is radioligand-specific, and for $[^{18}\text{F}]\text{FDG}$ is 40 minutes post-injection [15]. The AIF value at this time point is referred to here as AIF40. nSIME removes the need for acquiring any blood sample by incorporating a predicted value of AIF40 ($pAIF40$) as a constraint variable within its cost function. The predicted area under the curve of the AIF ($pAUC$), derived from the integration of the estimated AIF model, is introduced as a second constraint variable for nSIME to improve robustness and accuracy of the estimation process originally proposed [15]. While AIF40 describes one aspect of the AIF curve shape (tail height), the AUC captures characteristics of the global shape and scaling, and provides a more stable measure as it is calculated from multiple time points [17]. The soft constraint variables $pAIF40$ and $pAUC$ are incorporated into the nSIME cost function described in (2).

$$\begin{aligned} &\Phi(t, \theta^{PK}, \Psi_1^{tac}, \dots, \Psi_R^{tac}) \\ &= \sum_{r=1}^R \sum_{j=1}^J w_j [Y_{rj} - C(t_j|\theta, \Psi_r)]^2 \\ &+ v[pAIF40 - C_p(t_{opt}|\theta)]^2 + z[pAUC - AUC(\theta)]^2 \quad (2) \end{aligned}$$

The first term in Equation (2) minimizes over R ROIs and J time points the squared distance between the measured TAC, Y_{rj} , and the TAC predicted by the model, $C(t_j|\theta, \Psi_r)$, where θ and Ψ_r are the parameters of AIF and $[^{18}\text{F}]\text{FDG}$ kinetic models for the r^{th} ROI, respectively. The second term represents the soft constraint on AIF40, as the difference between $pAIF40$ and the corresponding value in the AIF model at time $t_{opt} = 40$ min, $C_p(t_{opt}|\theta)$. The third term is the soft constraint on AUC , given as the difference between $pAUC$ and the AUC of the AIF curve model $C_p(t|\theta)$. The weights v and z balance fitting of the observed TACs and adherence of the modeled AIF to the two constraints ($v = 100$ and $z = 5$, as suggested in [17]). As done previously for $[^{18}\text{F}]\text{FDG}$ [15], 5 ROIs (CER, CIN, HIP, PFC and PIP) were used within nSIME.

rCMRglu can then be estimated for each ROI from the Ψ_r estimated via nSIME as $rCMRglu = \frac{C_p}{LC} \frac{K_1 * k_3}{k_2 + k_3}$, where LC is the lumped constant (assumed equal to 0.65 here [25]) that converts rates of $[^{18}\text{F}]\text{FDG}$ uptake and phosphorylation into rates of glucose use, and K_1, k_2, k_3 are the micro-parameters of the $[^{18}\text{F}]\text{FDG}$ kinetic model in tissue.

G. Selection of EHR-Based Predictors

The soft constraint variables $pAIF40$ and $pAUC$ were predicted from EHR data only, using multiple linear regression models identified through a predictive algorithm. Initially, a screening procedure was applied to the whole set of EHR predictors (Table II) to select variables that are more strongly correlated to ground-truth measures $C_p(t_{opt}|\theta)$ and $AUC(\theta)$. The procedure uses squared Pearson's correlation coefficient, r^2 , in

linear regressions, with individual EHR variables as the predictors, and the ground-truth measure as the response variable.

This screening process is divided into 3 main steps [17], done separately for response variables $C_p(t_{opt}|\theta)$ and $AUC(\theta)$, thus obtaining a set of potential predictors for each constraint: 1) each predictor variable is retained if its correlation r^2 with the response variable is greater than 0.1; 2) each predictor variable is normalized for injected dose and retained if the correlation between the normalized and response variable is greater than the correlation between the injected dose itself and response variable; 3) all possible multiple regression models that include two predictors at a time are fitted with and without interaction terms, and the interaction term is selected if the correlation of the model with the interaction term is greater than the correlation of the model with only the two predictors. Furthermore, the r^2 of the model must be greater than 0.3 for $C_p(t_{opt}|\theta)$, and 0.4 for $AUC(\theta)$, and the p-value of the interaction term smaller than 0.05.

H. Predictive Model Design

We used a predictive algorithm previously described in [17], to separately predict $pAIF40$ and $pAUC$ from EHR data only using leave-one-out cross-validation. The aggregated model approach selects the regression model with the highest bootstrapped correlation to blood-based $mAIF40$ and $mAUC$ in the training data, each time excluding a different scan from the training set, and yields multiple models that are then aggregated to predict $pAIF40$ or $pAUC$. The number of predictors in each regression model was limited to two; three- and four- variable models were excluded in preliminary analyses, as they did not improve prediction accuracy, likely due to the small sample size.

I. Simulated Annealing

For each scan, nSIME ran using the subject-specific predicted $pAIF40$ and $pAUC$ values, without vascular correction of the TACs. Stochastic simulated annealing was used to solve the proposed optimization problem [15]. The nSIME-derived AIF with the smallest full width half maximum (FWHM) across 5 repeated runs was selected automatically for calculating rCMRglu. Five runs were used because, in some instances, it can take from 1 to 5 runs for SIME to converge to parameters that reconstruct an AIF curve with a typical physiological shape. AIF FWHM was calculated as the horizontal distance at mid height around the peak of the AIF curve. This helps to eliminate AIF curves with wide peaks.

J. Experimental Design and Evaluation Setup

First, we tested the performance of the aggregate model selection in estimating $pAIF40$ and $pAUC$. Constraint variables predictions were compared against the arterial blood-derived measured values ($mAIF40$ and $mAUC$) using Pearson's correlation coefficients and Bland-Altman (BA) plots. Second, we tested whether the PK-AIF model provides a better fit of the AIF curve and adds stability within nSIME compared to the 3E-AIF model used in [15], [16]. Performance was assessed by comparing Pearson's correlation coefficients from the regression analysis of rCMRglu estimates obtained with nSIME, using

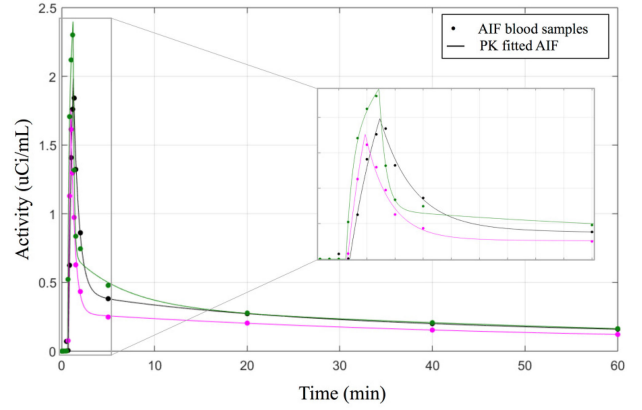


Fig. 1. Validation of PK-AIF modeling for [^{18}F]FDG. PK-AIF fitted curves $C_p(t|\theta)$ (solid lines) and AIF arterial blood samples (dots) for three different representative subjects (green, black, and magenta curves). The inset shows a detail of the AIF peak at 0–5 minutes.

either the 3E-AIF or PK-AIF model, with measured $mAIF40$ as the soft constraint variable, compared with using the gold standard blood-based AIF. Third, we tested whether adding the second soft constraint on $pAUC$ into the nSIME cost function improves performance. This was assessed via regression analysis of the rCMRglu estimates obtained by nSIME versus those obtained with AIF analysis, for the following scenarios: a) nSIME with measured $mAIF40$; b) nSIME with measured $mAIF40$ and $mAUC$; c) nSIME with predicted $pAIF40$; d) nSIME with predicted $pAIF40$ and $pAUC$. Fourth, we compared the performance of our method (nSIME with $pAIF40$ and $pAUC$) to that of the PBIF proposed in [23], by performing a regression analysis of rCMRglu estimated values of PBIF and our method versus values obtained with the gold standard. Finally, we estimated rCMRglu in two additional ROIs, parietal (PAR) and precuneus (PCN), which were not included among the regions used to estimate the nSIME AIF. We also compared the rCMRglu estimates across two diagnostic groups: healthy controls (CTR) and AD, using a two-sample t-test (significance level 0.05).

III. RESULTS

A. Quality of the PK Model for AIF Applied to [^{18}F]FDG

Fits of the PK model in (1) to blood-derived AIF samples are illustrated in Fig. 1 for three representative cases. Correlations of the derived constraint variables with blood-based values are: $r = 0.99$ for AIF40 and $r = 0.99$ for AUC. The range of values for the PK model parameters θ^{PK} obtained in the considered cohort were: t_d [0.49, 1] (min), T [0.19, 1] (min); B_1 [0, 0.5], B_2 [0.15, 0.9], B_3 [0.54, 2.91] ($\mu\text{Ci/mL}$); l_1 [0, 0.02], l_2 [0.21, 1.70], l_3 [0.54, 10] (min^{-1}).

B. Performance of Predictor Selection

The screening procedure selected a total of 40 predictors for $pAIF40$ and 38 for $pAUC$ (frequently selected predictors are reported in Table III). TACsum, RDW, and ID were frequently selected for both constraint variables. Other frequent predictors included triglycerides for $pAIF40$, and BSA and ColdGlu2 for $pAUC$. The aggregate model approach yielded the following correlation values between predicted and blood-based values:

TABLE III
FREQUENCY OF PREDICTOR VARIABLES APPEARANCE IN MODELS
SELECTED BY THE AGGREGATE-MODEL
PREDICTIVE APPROACH

Predicted constraint	Predictor variable	Frequency (%)
pAIF40	TACsum	35.5
	RDW	31.1
	Triglyceride	27.9
	Injected Dose	4.9
pAUC	TACsum	37.0
	RDW	25.0
	Injected Dose	12.1
	BSA	7.3
	ColdGlu2	6.6
	eTPV	4.3
	eRMR	3.4

Only variables with a frequency greater than 3.0% are shown

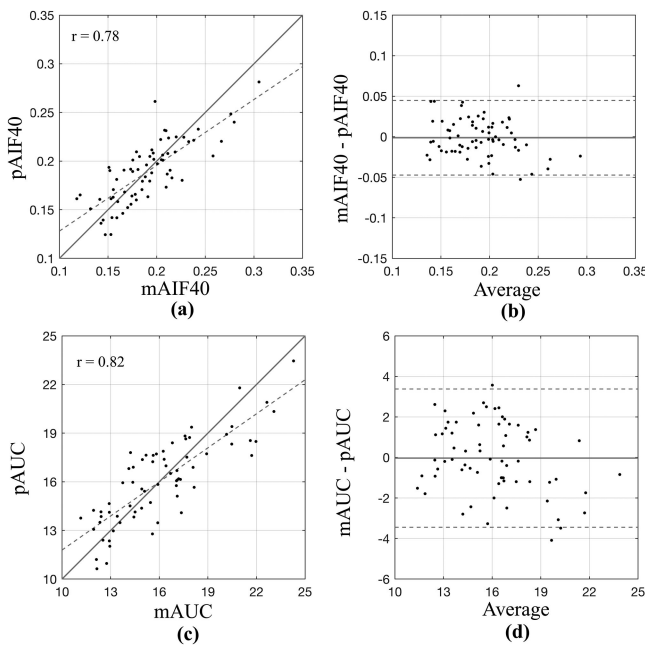


Fig. 2. Predictive modeling results with the aggregate model. Regression (a), (c) and BA (b), (d) plots of predicted versus ground-truth values from AIF arterial blood samples. (a), (b) Predicted AIF40 (*pAIF40*) versus measured AIF40 (*mAIF40*). (c), (d) Predicted AUC (*pAUC*) versus measured AUC (*mAUC*). Regression plots: identity line (solid); regression line (dashed). BA plots: solid line is the mean; dashed line is the mean $\pm 1.96 \times$ (standard deviation).

$r = 0.78$ (*pAIF40*) and $r = 0.82$ (*pAUC*). Results of the predictions are reported in Fig. 2 as scatter plots and as BA plots.

C. PK-AIF Versus 3E-AIF

Using the PK-AIF model improves correlation between nSIME with measured *mAIF40* and gold standard rCMRglu values ($r = 0.90$) compared to the 3E-AIF model ($r = 0.85$), and yields a smaller bias, closer to 0 (Fig. 3). Notably, there are also fewer outlier errors when the PK-AIF model is used.

D. Using One Versus Two Constraints

Using nSIME with blood-based soft constraint values leads to correlations between nSIME-derived and AIF-based rCMRglu values of $r = 0.90$ when using only *mAIF40* (Fig. 4(a)–(b) and

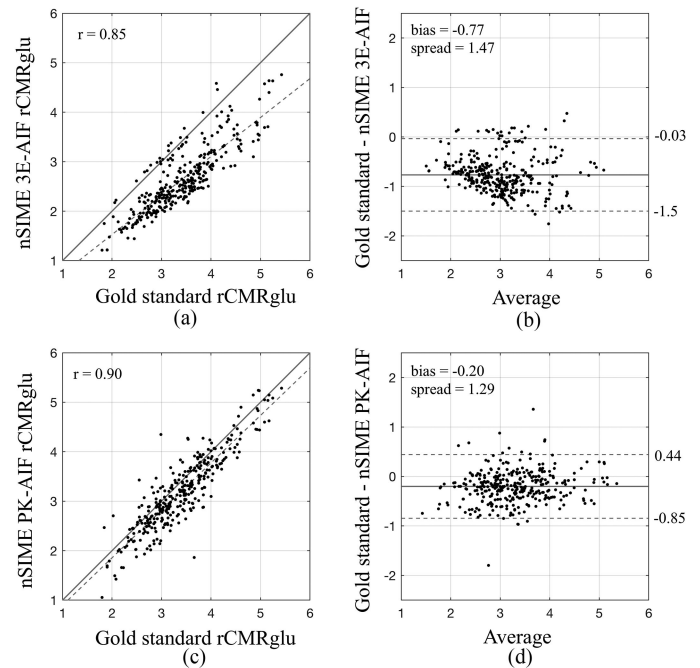


Fig. 3. TAC rCMRglu estimations using nSIME modeling with the ground-truth *mAIF40* as the constraint variable. Regression (a), (c) and Bland-Altman (b), (d) plots are displayed for: (a), (b) rCMRglu obtained with the 3E-AIF model; (c), (d) rCMRglu obtained with the PK-AIF model. Regression plots: identity line (solid), regression line (dashed). BA plots: solid line is the mean, dashed line is the mean $\pm 1.96 \times$ (standard deviation).

$r = 0.94$ when using both *mAIF40* and *mAUC* (Fig. 4(c)–(d)). Moreover, the spread between the 95% limits of agreement in the BA plots is reduced from 1.29 to 1.01 when using two soft constraints, while biases are similar and close to 0. Using nSIME with non-invasively predicted soft constraint variables leads to correlations between nSIME-derived and AIF-based rCMRglu values of $r = 0.79$ when using only *pAIF40* (Fig. 5(a)–(b)), and $r = 0.83$ when using both *pAIF40* and *pAUC* (Fig. 5(c)–(d)). The BA plots spread is reduced from 1.72 to 1.55 when using two soft constraints, with a slightly higher bias equal to 0.15.

E. Comparison of nSIME With the PBIF Approach

rCMRglu estimates obtained using the population approach proposed in [23] are reported in Fig. 6. Compared to nSIME, with two predicted soft constraint variables, correlation is lower for PBIF (0.77 vs. 0.83), spread is higher (2.12 vs. 1.55), and bias is higher (0.43 vs. 0.15).

F. Individual ROI and Group Analyses

Correlation between rCMRglu estimated values with nSIME and those obtained using the gold standard blood-based approach are $r = 0.759$ and $r = 0.768$ for PAR and PCN, respectively, comparable to individual correlations for the five ROIs used to estimate the nSIME AIF, $r = 0.693$ – 0.798 .

There is a significant difference in rCMRglu between CTR and AD groups: for the gold standard approach, CIN ($p = 0.015$), PAR ($p = 0.0004$), and PCN ($p = 0.0005$); for nSIME, CIN ($p = 0.016$), PAR ($p = 0.00006$), and PCN ($p = 0.0002$).

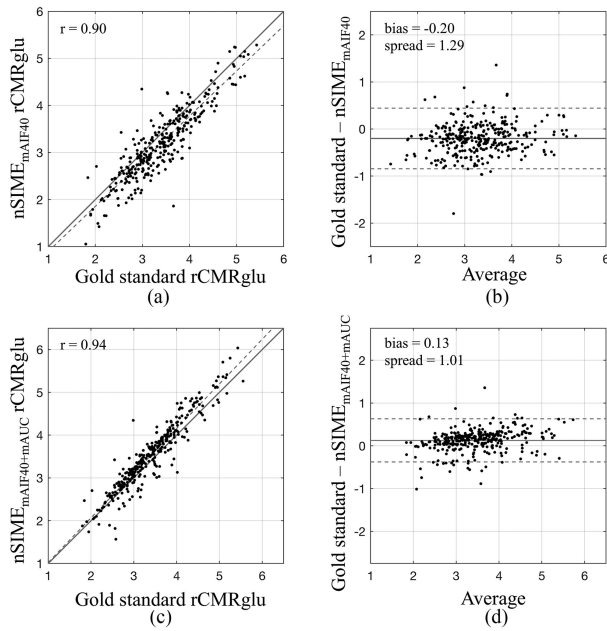


Fig. 4. TAC rCMRglu estimations using PK-AIF nSIME with one or two ground-truth soft constraint variables. Regression (a), (c) and BA (b), (d) plots are displayed for: (a), (b) nSIME with $mAIF40$; (c), (d) nSIME with both $mAIF40$ and $mAUC$. Regression plots: identity line (solid), regression line (dashed). BA plots: solid line is the mean, dashed line is the mean $\pm 1.96\sigma$ (standard deviation).

IV. DISCUSSION

In this study we extended the use of nSIME to [^{18}F]FDG, with the goal of eliminating the need for arterial blood sampling during PET scanning. Our results indicate that the nSIME framework can accurately quantify rCMRglu from [^{18}F]FDG data, outperform the population based approach, and achieve comparable group discrimination to the gold standard.

High correlations with arterial blood-derived values were achieved with the aggregate predictive model from [17]. The predictors that most frequently appeared for both constraints were TACsum, RDW, and ID. Triglycerides were also frequently included for prediction of $pAIF40$, whereas weight/height-derived variables (e.g., BSA, eRMR, eTPV) and ColdGlu2 were more important for predicting $pAUC$. The ID is directly related to the distribution of the radioligand in the blood. BSA may impact the volume of blood into which the radioligand is diluted, and has been used in the past as a normalization factor for the AIF [10], [26] and to predict other blood-related anchor values [16]. Notably, the relationship between weight/height-derived variables and AUC has already been identified in [17] for [^{11}C]DASB. An interesting finding is the selection of RDW and triglycerides, which were not identified as predictors for [^{11}C]DASB. One possible explanation is that RDW is related to metabolic balance and red blood cell homeostasis [27] and thus partially reflects each subjects' metabolic profile. Triglycerides have been associated with inflammation-related [^{18}F]FDG uptake in arterial plaques [28], which could influence blood availability of the radioligand, especially in the older MCI and AD subjects in this study. Triglycerides may also affect lipid membrane composition and thus a variety of cellular functions that in turn could impact glucose uptake and utilization. Finally, unlike [^{11}C]DASB, HR and BP do not appear to be relevant for

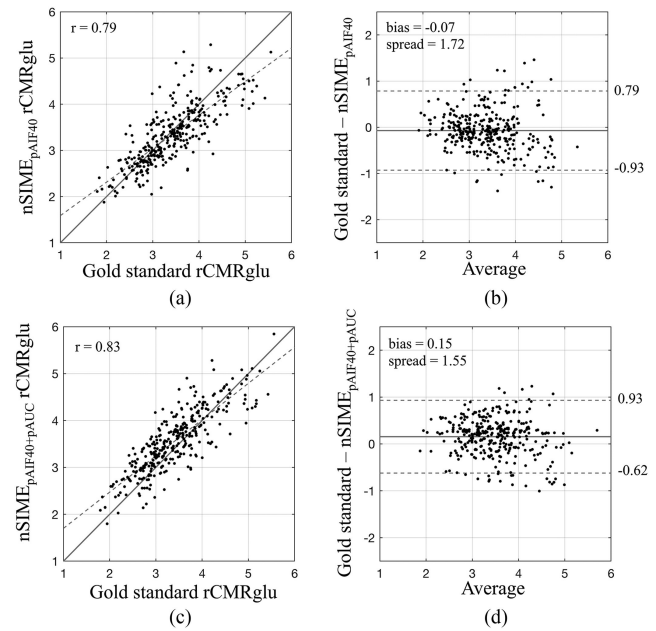


Fig. 5. TAC rCMRglu estimations using PK-AIF nSIME with one or two predicted soft constraint variables. Regression (a), (c) and BA (b), (d) plots are displayed for: (a), (b) nSIME with $pAIF40$; (c), (d) nSIME with both $pAIF40$ and $pAUC$. Regression plots: identity line (solid), regression line (dashed). BA plots: solid line is the mean, dashed line is the mean $\pm 1.96\sigma$ (standard deviation).

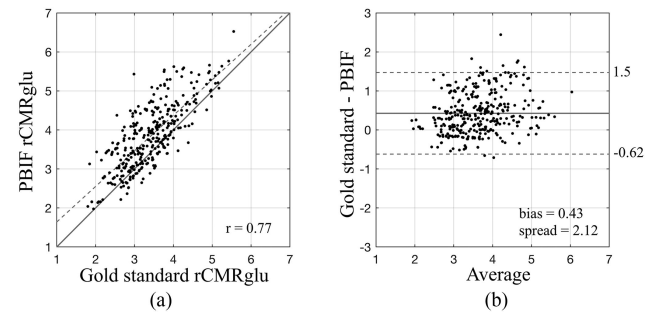


Fig. 6. TAC rCMRglu estimations using the population-based approach. Regression (a) and BA plots (b) are shown. Regression plots: identity line (solid), regression line (dashed). BA plots: solid line is the mean, dashed line is the mean $\pm 1.96\sigma$ (standard deviation).

[^{18}F]FDG-based prediction, possibly because [^{18}F]FDG is metabolized throughout the body whereas [^{11}C]DASB is primarily metabolized by the liver.

It should be noted that both data collection and subject inclusion criteria were not specifically designed for this retrospective analysis. Furthermore, EHR data used in this study were gathered within hours to months before the PET scan, therefore limiting the accuracy of our analysis. A prospective data collection could contribute to even more accurate prediction and to fewer outliers, thus improving overall performance of the proposed non-invasive method.

In a separate analysis (data not shown), we compared the performance of the aggregate model with that of a simplified approach, which selects just a single regression model with the highest bootstrapped correlation. We found that the aggregate model yields slightly better performance, consistent with our previous results with [^{11}C]DASB.

Our findings support the use of the PK-AIF model rather than a 3E-AIF model, as it yields an improvement in nSIME performance itself. The inclusion of the AUC as a second soft constraint into the nSIME cost function significantly improved the algorithm performance for estimating rCMRglu. Indeed, constraining not only the AIF at a specific time point (AIF40), but also its overall AUC, aids in accurately reconstructing the shape of each individual AIF curve, making nSIME a more personalized approach compared to other methods for non-invasive estimation of AIF. nSIME also outperformed the PBIF approach, showing higher correlation and lower spread and bias in the rCMRglu estimates vs. gold standard values.

Individual ROI results show that nSIME is applicable to ROIs beyond those that are used to estimate the AIF. Group analyses suggest that discrimination between CTR and AD is comparable between nSIME and the gold standard.

The technical contributions presented here enabled nSIME to be adapted for accurate quantification of the [^{18}F]FDG radioligand, by demonstrating that using two constraints, the PK-AIF model, and the AIF curve shape selection improves overall performance against the gold standard and also outperforms a non-invasive population-based approach. nSIME shows potential for future research and clinical application, as it eliminates the need for arterial blood sampling or for the estimation of spillover and recovery coefficients as in the case of IDIF methods.

V. CONCLUSION

We propose a totally non-invasive nSIME approach for the estimation of [^{18}F]FDG rCMRglu values from brain PET images that takes advantage of pharmacokinetic theory, health record data and predictive algorithms. The advantage of using nSIME over a population-based input function approach is demonstrated. The high correlation values and small bias in quantification errors support the applicability of nSIME to the widely used [^{18}F]FDG radioligand and should be investigated further in specific prospective studies and additional radioligands. Our results advocate for the development of larger databases of PET images, and of radioligand blood sampling and EHR data, as part of a more general push toward a big-data approach in quantitative PET imaging.

REFERENCES

- [1] T. Jones and E. Rabiner, "The development, past achievements, and future directions of brain PET," *J. Cerebral Blood Flow Metabolism*, vol. 32, pp. 1426–1454, 2012.
- [2] R. A. J. O. Dierckx, A. Otte, E. F. J. de Vries, A. van Waarde, and J. A. den Boer, *PET and SPECT in Psychiatry*. New York, NY, USA: Springer, 2014.
- [3] D. Delbeke, "Oncological applications of FDG PET imaging: Brain tumors, colorectal cancer lymphoma and melanoma," *J. Nucl. Med.*, vol. 40, no. 4, pp. 591–603, 1999.
- [4] L. Mosconi *et al.*, "Multicenter standardized ^{18}F -FDG PET diagnosis of mild cognitive impairment, Alzheimer's disease, and other dementias," *J. Nucl. Med.*, vol. 49, no. 3, pp. 390–398, 2008.
- [5] S. S. Gambhir *et al.*, "A tabulated summary of the FDG PET literature," *J. Nucl. Med.*, vol. 42, no. S5, pp. 1S–93S, 2001.
- [6] L. K. Shankar *et al.*, "Consensus recommendations for the use of ^{18}F -FDG PET as an indicator of therapeutic response in patients in National Cancer Institute Trials," *J. Nucl. Med.*, vol. 47, pp. 1059–1066, 2006.
- [7] K. Chen *et al.*, "Noninvasive quantification of the cerebral metabolic rate for glucose using positron emission tomography, ^{18}F -fluoro-2-deoxyglucose, the Patlak method, and an image-derived input function," *J. Cerebral Blood Flow Metabolism*, vol. 18, no. 7, pp. 716–723, 1998.
- [8] P. Zanotti-Fregonara, K. Chen, J.-S. Liow, M. Fujita, and R. B. Innis, "Image-derived input function for brain PET studies: Many challenges and few opportunities," *J. Cerebral Blood Flow Metabolism*, vol. 31, no. 10, pp. 1986–1998, 2011.
- [9] M. Bentourkia, "Kinetic modeling of PET-FDG in the brain without blood sampling," *Comput. Med. Imag. Graph.*, vol. 30, pp. 447–451, 2006.
- [10] T. Shiozaki *et al.*, "Noninvasive estimation of FDG input function for quantification of cerebral metabolic rate of glucose: Optimization and multicenter evaluation," *J. Nucl. Med.*, vol. 41, pp. 1612–1618, 2000.
- [11] S. Takagi *et al.*, "Quantitative PET cerebral glucose metabolism estimates using a single non-artificialized venous-blood sample," *Ann. Nucl. Med.*, vol. 18, no. 4, pp. 297–302.
- [12] S. Takikawa *et al.*, "Noninvasive quantitative fluorodeoxyglucose PET studies with an estimated input function derived from a population-based arterial blood curve," *Radiology*, vol. 188, no. 1, pp. 131–136, 1993.
- [13] F. O'Sullivan *et al.*, "Kinetic quantitation of cerebral PET-FDG studies without concurrent blood sampling: Statistical recovery of the arterial input function," *IEEE Trans. Med. Imag.*, vol. 29, no. 3, pp. 610–624, Mar. 2010.
- [14] A. Bertoldo, G. Rizzo, and M. Veronese, "Deriving physiological information from PET images: From SUV to compartmental modelling," *Clin. Transl. Imag.*, vol. 2, no. 3, pp. 239–251, 2014.
- [15] R. T. Ogden, F. Zanderigo, S. Choy, J. J. Mann, and R. V. Parsey, "Simultaneous estimation of input functions: An empirical study," *J. Cerebral Blood Flow Metabolism*, vol. 30, no. 4, pp. 816–826, 2009.
- [16] F. Zanderigo, R. T. Ogden, and R. V. Parsey, "Noninvasive blood-free full quantification of positron emission tomography radioligand binding," *J. Cerebral Blood Flow Metabolism*, vol. 35, pp. 148–156, 2015.
- [17] A. Mikhno *et al.*, "Toward non-invasive quantification of brain radioligand binding by combining electronic health records and dynamic pet imaging data," *IEEE J. Biomed. Health Inform.*, vol. 19, no. 4, pp. 1271–1282, Jul. 2015.
- [18] E. Rocca *et al.*, "Non-invasive quantification of brain [^{18}F]FDG uptake by combining medical health records and dynamic PET imaging data," in *Proc. 37th Annu. Int. Conf. IEEE Eng. Med. Biol. Soc.*, Milan, Italy, 2015, pp. 2243–2246.
- [19] D. P. Devanand *et al.*, "Pittsburgh compound B (^{11}C -PIB) and fluorodeoxyglucose (^{18}F -FDG) PET in patients with Alzheimer disease, mild cognitive impairment, and healthy controls," *J. Geriatric Psychiatry Neurol.*, vol. 23, no. 3, pp. 185–198, 2010.
- [20] H. Duvernoy, *The Human Brain: Surface, Three-Dimensional Sectional Anatomy and MRI*. New York, NY, USA: Springer-Verlag Wien, 1991.
- [21] D. Devanand, G. Pradhaban, and X. Liu, "Hippocampal and entorhinal atrophy in mild cognitive impairment: Prediction of Alzheimer disease," *Neurology*, vol. 68, no. 11, pp. 828–836, 2007.
- [22] A. Mikhno *et al.*, "Combining brain imaging data with electronic health records to non-invasively quantify [^{11}C]DASB binding," in *Proc. IEEE Int. Conf. Biomed. Health Inform.*, 2014, pp. 732–735.
- [23] D. Vriens, L.-F. de Geus-Oei, W. J. G. Oyen, and E. P. Visser, "A curve-fitting approach to estimate the arterial plasma input function for the assessment of glucose metabolic rate and response to treatment," *J. Nucl. Med.*, vol. 50, no. 12, pp. 1933–1939, 2009.
- [24] L. Sokoloff *et al.*, "The [^{14}C]deoxyglucose method for the measurement of local cerebral glucose utilization: Theory, procedure, and normal values in the conscious and anesthetized albino rat," *J. Neurochem.*, vol. 28, no. 5, pp. 897–916, 1977.
- [25] H. M. Wu *et al.*, "Measurement of the global lumped constant for 2-Deoxy-2- ^{18}F fluoro-D-glucose in normal human brain using [^{15}O]water and 2-deoxy-2- ^{18}F fluoro-D-glucose positron emission tomography imaging: A method with validation based on Multiple methodologies," *Mol. Imag. Biol.*, vol. 5, no. 1, pp. 32–41, 2003.
- [26] T. Tsuchida, N. Sadato, Y. Yonekura, and S. Nakamura, "Noninvasive measurement of cerebral metabolic rate of glucose using standardized input function," *J. Nucl. Med.*, vol. 40, no. 9, pp. 1441–1445, 1999.
- [27] G. L. Salvagno, "Red blood cell distribution width: A simple parameter with multiple clinical applications," *Crit. Rev. Clin. Lab. Sci.*, vol. 52, no. 2, pp. 86–105, 2015.
- [28] D. N. Chroinin *et al.*, "Serum lipids associated with inflammation-related PET-FDG uptake in symptomatic carotid plaque," *Neurology*, vol. 82, no. 19, pp. 1693–1699, 2014.